Performance Characteristics of STIS Detectors
NASA Contract NAS5-30435

IN-33-CR

Final Report

137102

P.50

Submitted To:

National Aeronautics and Space Administration
Goddard Space Flight Center
Greenbelt Road
Greenbelt, MD 20771

Principal Investigator:

Robert A. Stern

Dept 91-30 Bldg 252

Lockheed Palo Alto Research Laboratory

3251 Hanover St.

Palo Alto, CA 94304

(415) 424-3272

December 31, 1992

NASA

Report Documentation Page

1. Report No.	2. Government Accession No.	3. Recipient's Catalog No.
4. Title and Subtitle PERFORMANCE CHARACTERISTICS OF STIS DETECTORS		**5. Report Date** DECEMBER 31, 1992
		6. Performing Organization Code
7. Author(s) ROBERT A. STERN		**8. Performing Organization Report No.**
		10. Work Unit No.
9. Performing Organization Name and Address LOCKHEED PALO ALTO RESEARCH LABORATORY 3251 Hanover Street Palo Alto, CA 94304-1191		**11. Contract or Grant No.** NAS5-30435
12. Sponsoring Agency Name and Address NASA Goddard Space Flight Center		**13. Type of Report and Period Covered** 9-01-88 -- Final Report 12-31-92
		14. Sponsoring Agency Code

15. Supplementary Notes

16. Abstract

We report quantum efficiency measurements of back-illuminated, ion-implanted, laser-annealed charge coupled devices (CCDs) in the wavelength range 13–10,000 Å. The equivalent quantum efficiency (EQE=effective photons detected per incident photon) ranges from a minimum of 5% at 1216Å to a maximum of 87% at 135 Å. Using a simple relationship for the charge collection efficiency of the CCD pixels as a function of depth, we present a semi-empirical model with few parameters which reproduces our measurements with a fair degree of accuracy. The advantage of this model is that it can be used to predict CCD QE performance for shallow backside implanted devices without detailed solution of a system of differential equations, as in conventional approaches, and yields a simple analytic form for the charge collection efficiency which is adequate for detector calibration purposes. Making detailed assumptions about the dopant profile, we also solve the carrier density and continuity equations in order to relate our semi-empirical model parameters to surface and bulk device properties. The latter procedure helps to better establish device processing parameters for a given level of CCD QE performance.

17. Key Words (Suggested by Author(s)) Charge Coupled Devices, Ultra Violet	18. Distribution Statement Unclassified -- Unlimited		
19. Security Classif. (of this report) Unclassified	20. Security Classif. (of this page) Unclassified	21. No. of pages	22. Price

NASA FORM 1626 OCT 86

Abstract

We report quantum efficiency measurements of back-illuminated, ion-implanted, laser-annealed charge coupled devices (CCDs) in the wavelength range 13–10,000 Å. The equivalent quantum efficiency (EQE=effective photons detected per incident photon) ranges from a minimum of 5% at 1216Å to a maximum of 87% at 135 Å. Using a simple relationship for the charge collection efficiency of the CCD pixels as a function of depth, we present a semi-empirical model with few parameters which reproduces our measurements with a fair degree of accuracy. The advantage of this model is that it can be used to predict CCD QE performance for shallow backside implanted devices without detailed solution of a system of differential equations, as in conventional approaches, and yields a simple analytic form for the charge collection efficiency which is adequate for detector calibration purposes. Making detailed assumptions about the dopant profile, we also solve the carrier density and continuity equations in order to relate our semi-empirical model parameters to surface and bulk device properties. The latter procedure helps to better establish device processing parameters for a given level of CCD QE performance.

Contents

1 INTRODUCTION

Since the mid 1980's, there has been a concerted effort to produce a back-illuminated CCD with high quantum efficiency (QE) in the ultraviolet (UV) and extreme ultraviolet (EUV) range for space flight and other applications (100–4000 Å) (Bosiers *et al.* 1986, Janesick *et al.* 1987, Stern *et al.* 1987, Tassin *et al.* 1989). In the region below 1050 Å, where window materials such as MgF_2 no longer transmit appreciably, techniques used in ground-based astronomy with sealed detector systems, which are dependent upon control of the ambient environment, such as the UV flood (Janesick *et al.* 1985), are no longer viable. Also, in the soft X-ray regime, at wavelengths short of the Si $L_{2,3}$ edge at 121 Å, or between 40–120 Å, the absorption path in silicon become small enough (< 1000 Å) that stability and charge collection efficiency become serious issues for back-illuminated CCDs. To alleviate these concerns and produce a stable, high QE device throughout the soft X-ray, EUV, and UV regions, one technique being vigorously pursued at present is the use of ion implantation in conjunction with laser annealing (Stern *et al.* 1989, Bailey *et al.* 1990, Hochedez 1992).

This technique owes much to earlier work in the field of laser annealing of implanted silicon in general (see, e.g., Young *et al.* 1978, Poate and Mayer 1982), and, in particular, annealing of implanted solar cells (e.g., Katzeff *et al.* 1981). In the area of solar cell research, much effort has also gone into the development of analytical and numerical solutions to photogenerated charge transport in heavily doped ($N_A \gtrsim 10^{17}$ cm^{-3}) implanted regions in the solar cell (del Alamo and Swanson 1987, Cuevas and Balbuena 1989, Bisschop *et al.* 1990). This modeling approach has been directly applied to laser annealed CCDs by Bailey *et al.* (1990) and Hochedez *et al.* (1992) to model CCD quantum efficiencies in the soft X-ray region. Blouke (1991) has also developed an analytic model of a thinned CCD using generalized parameters for a back surface field in the form of a step function.

In this paper, we report quantum efficiency measurements and derived charge-collection

efficiencies for ion-implanted, laser-annealed Tektronix 512 x 512 back-illuminated CCDs developed under a NASA sponsored cooperative research program between Lockheed Palo Alto Research Laboratory (LPARL) and Tektronix, Inc. The quantum efficiencies, taken over a broad wavelength band from the soft X-ray (13 Å) to the near IR (1 μm), are used to constrain model parameters based upon a semi-empirical charge-collection efficiency (CCE) model, which assumes that the differential CCE is a linear function of distance from the back CCD surface. We also compare our results in the context of more formal models of the charge collection efficiency in order to relate the semi-empirical model parameters to those usually described in the semiconductor literature. A model of CCD reflectivity and absorption developed at Lockheed Palo Alto Labs is also used in the overall quantum efficiency calculation.

2 CCD PROCESSING

The CCDs discussed in this paper are all Tektronix TK512CB 512 x 512 pixel back-illuminated CCDs which have been specially processed for this project. The processing steps are as follows: (1) up to and including the frontside circuitry processing and the backside thinning process, all wafers are fabricated using standard production line methods for the TK512CB back-illuminated CCD, (2) after thinning, the back surfaces of the wafers are implanted by Tektronix with 10 keV BF_2 at various implant doses (see discussion below), (3) at this point the wafers are shipped to Lockheed Palo Alto, where they are laser annealed using a pulsed Nd:Glass laser with a frequency doubler. The frequency doubler puts approximately 25% of the beam power into a green wavelength (5300 Å), with the remaining 75% of power at the 1.06 μm primary laser wavelength. The laser beam is directed through a fused silica "homogenizer" rod (Cullis, Webber, and Bailey 1978) which reduces beam non-uniformity. The laser pulse is $\approx$ 20 nsec. The short pulse length provides optimum conversion efficiency for the frequency doubler. The wafer is masked using a stainless steel fixture provided by Tektronix which protects the back-side bond pads from the laser. Laser anneal energy densities were optimized via a procedure described in §4. (4) the laser annealed wafer is returned to Tektronix for dicing, packaging, and functional testing. (5) after diode-mode visible light quantum efficiency tests by Tektronix (§3.1), the packaged devices are shipped to Lockheed for UV, EUV, and X-ray measurements. No anti-reflection coating or conductive layers are applied to the back surface, which consists of the native oxide ($\sim$20–50 Å) overlying the thinned, implanted and annealed silicon substrate.

In this paper, we will be describing measurements and QE modeling for devices produced in two wafer lots. The first lot, #1229, proved to be primarily a trial run which was useful in correcting a serious nonuniformity problem with our homogenizer(§4). The second lot, #1302, proved to be much more, though not completely, uniform. Characteristics of four

devices for which most of the measurements were taken are given in Table 1.

Table 1: Implant and Laser Anneal Process Parameters / Wafers implanted with 10 kev BF_2

Device Serial #	Implant Dose (10^{15} cm^{-2})	Nominal Anneal Energy Density (J cm^{-2})	Comments
1229-1-6	2.0	1.06	Highly non-uniform
1229-7-2	1.0	1.1	Highly non-uniform
1302-7-9	1.0	1.32	
1302-7-12	1.0	1.39	

3 EXPERIMENT

3.1 Visible Light Diode Testing

The quantum efficiency was measured at room temperature using the device as a large area photodiode. All gates were grounded and the input and output diodes, i.e., the connections to the CCD buried channel, were coonnected in parallel and subsequently connected to the input of a Keithley 1197 picoammeter. The current measurements were made at zero bias on the channel.

The device was mounted in a ZIF (zero insertion force) socket at one end of a long blackened enclosure. A NIST traceable UDT photodiode was permanently mounted in the enclosure next to the ZIF socket and in the same plane as the test device. Light was introduced to the enclosure through a 5 cm square opening in the wall opposite the test device. The source was a Tungsten-Halogen lamp. Between the source and the test chamber was a small chamber which contained two ground glass diffuser plates and a slot into which the appropriate filters could be placed to limit the spectral content of the source. The filters were interference coated filters with 10 nm bandwidth and spaced at 50 nm as indicated in the data.

The CCD quantum efficiency was calculated by comparing the output from the known test diode with the signal obtained simultaneously from the test device. Knowing the relative areas of the two devices and the quantum efficiency of the diode allows one to compute the quantum efficiency of the CCD using the following equation:

$$\eta_{CCD} = \eta_{diode} * \frac{J_{CCD}}{J_{diode}} * \frac{A_{diode}}{A_{CCD}}$$

The area of the diode was 1.0 cm^2 and the effective area of the CCD is assumed to be the sum of the imaging area and the serial registers. J_{CCD} and J_{diode} are the measured

currents and η_{diode} is the NIST traceable quantum efficiency of the diode.

3.2 LPARL CCD Camera System

UV, EUV, and X-Ray measurements at LPARL were carried out using a low-contamination camera head and vacuum system in our laboratory (Shing *et al.* 1991). The vacuum chamber and camera head are designed to operate in an organic-free hard vacuum of $\approx 4 \times 10^{-8}$ torr or less, achieved by careful materials control and a clean turbopump system. The camera head is capable of cooling the CCD to temperatures as low as -110 C with stability on the order or ± 0.1 C over a few hours, and ability to set the temperature to within about 0.5 C of any desired value. We typically operated the CCD at -70 C, which was sufficient to keep dark current to $\lesssim 0.5$ $e^-s^{-1}pix^{-1}$. The noise in the camera system is limited primarily by read noise in the CCD, and some additional noise produced by the high frequency circuits in the turbopump. Even so, the devices operated with a total read noise of 15-20 e^-pixel^{-1}, with a contribution of ≈ 10-$15e^-$ from the CCD, and the additional nose from the turbopump. This noise floor, though not extremely low by today's CCD technology (Janesick *et al.* 1987b), is still a negligible factor in our QE measurements (see §5).

A Princeton Scientific Instruments Model V system served as the camera head and readout electronics. An IBM AT running FORTH controlled the camera system. Images from the IBM were transferred to a Silicon Graphics 4D/310 Unix-based server for further analysis.

3.3 LPARL Blue/UV Measurement System

Measurements of the CCD QE and uniformity were carried out at 3 blue/UV Hg lamp lines: 2537, 3650, and 4050 Å. The experimental setup was similar to that described in Stern *et al.* (1989), with an Hg lamp, narrow-band interference filters for the Hg lines, an optical

diffuser, and sapphire chamber window. This resulted in a (nearly) flat-field illumination of the CCD. The absolute QE was determined by pre-calibrating the Hg lamp setup with a pair of UDT UV-100 photodiodes, one placed on a rotatable arm near the front end of the vacuum chamber close to the illumination source, and a second temporarily placed at the CCD position. The ratio of signals at each photodiode was taken with the Hg lamp at each wavelength (the ratio did not change with wavelength, as expected), the temporary diode removed, and the CCD camera head reaffixed to the chamber. By monitoring the current on the rotatable-arm diode before and after each exposure, we were able to convert to the absolute beam illumination at the CCD using the previously determined diode ratio. The absolute QE of the diode is ultimately derived from NIST standards: for 3650 and 4050. Å, we used the manufacturers calibration, while for 2537 Å, we performed our own calibration, using a Ball Aerospace MgF_2 window/ CsTe photocathode sealed UV photodiode calibrated by NIST to an absolute accuracy of $\approx$ 10%. For each CCD QE measurement, diode current readings were taken using a Keithley model 617 digital electrometer both before and after each 5-10 sec Hg lamp exposure. For the range of currents measured ($\sim$ 0.5–4.0 nA), the typical 1σ uncertainty was $\sim$ 1%.

3.4 EUV and Soft X-Ray Measurement System

For wavelengths below 2000 Å, requiring windowless operation in high vacuum, we performed calibrations using the LPARL Calibration Facility, described in detail by Windt *et al.* (1988). The calibration facility is shown schematically in Figure 1 . A hollow-cathode discharge designed and built at LPARL, and based on the earlier work of Paresce *et al.* (1971) and Manson (1973) is used in the wavelength range above 200 Å, and a Manson Model 2 X-ray source is used to excite characteristic X-ray lines in the 13.6 - 171 Å region. A 1m McPherson grazing incidence monochromator with gratings of either 300 or 600 g/mm is used to isolate individual strong lines. The output of the monochromator is partially

collimated by a paraboloidal grazing incidence mirror into a beam of dimension a few mm in size. The beam traverses a large reflectometer chamber, which we use primarily for the purpose of inserting various reference calibration detectors: NIST windowless diodes, a microchannel plate, or a thin-window gas flow proportional counter purchased from the J.E. Manson company. For the wavelength range above 200 Å, the microchannelplate(MCP) is used as a secondary standard, after having been calibrated against the NIST diode. Since we have concerns over possible diode efficiency changes, we actually use two NIST diodes, one of which is kept in the vacuum chamber, and a second is kept stored in a dry box except during short (1 day or less) calibration runs to check the stability of the diode kept in vacuum.

The proportional counter is used with a fill gas (either P-10 or P-50, depending upon the wavelength) such that soft X-rays are essentially completely absorbed in the counter volume. Calibration of the counter is then a matter of window calibration, We performed window transmission calibrations at all soft X-ray wavelengths used: these calibrations are good to a few % or better. At the longest wavelength for which the proportional counter is used, 171 Å, the pulse-height spectrum of the counter is broad and counts may be lost at the low end of the discriminator threshold. We therefore regard the measurements at this wavelength as upper limits to the true CCD efficiencies. We estimate this effect to be no greater than 5-10%, based upon the shape of the PHA spectrum.

4   OPTIMIZATION OF IMPLANT AND ANNEAL PARAMETERS

Optimization of implant dose and anneal energy density was initially carried out using a set of bare Si (100) n-type wafers implanted with various BF_2 doses from $\approx 1 \times 10^{14}$–5×10^{15} cm^{-2}. The Nd:Glass pulsed laser anneal requires an amorphized Si surface for optimum coupling of the green and IR energies in order to produce liquid phase epitaxial growth at minimal energy densities thus reducing implant redistribution (Katzeff *et al.* 1981). Thus, it rapidly became clear that the lowest implant doses were not suitable. Also, the highest implant doses appeared to couple so strongly to the anneal pulse that surface damage appeared on the test wafers. SIMS (Secondary Ion Mass Spectrometry) and spreading resistance measurements were used to determine a nominally optimum set of implant parameters from these test wafers.

The other factor in this process is, of course, the anneal beam pattern and energy density. In our initial work, we measured only the total power in the laser anneal beam and the green fraction, assuming, on the basis of earlier measurements with the same laser anneal system, that the beam emerging from the fused silica homogenizer was quite uniform. It turned out, however, that the homogenizer had developed damage spots on its surface which introduced significant non-uniformities in the output beam. Thus our first set of test 512 x 512 devices (from lot 1229) had a highly non-uniform UV quantum response. This turned out to be a blessing in disguise, however, as the UV response pattern correlated quite well with the laser anneal beam pattern, which we remeasured using a 100 x 100 Reticon array (with IR and green filters separately).

An example of this correlation is shown in Figure 2 , which is an image of device 1229-7-2 exposed to a relatively uniform illumination of 2537Å light from a Hg pen lamp and interference filter. Darker shades of gray represent higher values of QE. Superimposed on this gray-scale image are contours of equal anneal energy density measured using the

100x100 Reticon array and corrected for the proper proportion of green and IR light. The contours of anneal beam energy density were determined by measuring the total beam power in Joules/pulse (which varied by a few %), and integrating the green and IR Reticon images over the entire beam, attributing 25% of the total power to the green beam, as determined in earlier measurements. The resulant image was then scaled to the proper size, and then translated to to the point providing the strongest anti-correlation with the CCD image intensities.

The spatial correlation is quite obvious, as is the fact that the the optimum anneal energy density, which produces the highest UV response, occurs at ≈ 1.3 J cm^{-2}, Thus this device provides, in effect, a guide to optimizing the energy density for a refurbished homogenizer system with a more uniform energy density. Given pulse-to-pulse reproducibility, various measurement errors, etc., we still allowed for a $\pm 20\%$ uncertainty in the absolute value of the energy density in the actual processing run.

In order to achieve the required uniformity, we fabricated a new homogenizer rod of the same diameter and approximate length. We discovered, however, that we were not able to eliminate completely the focusing effects of the rod bend, which produced residual non-uniformities in the anneal pulse Reticon images (see Figure 3). However, the wide variation in anneal energy density was substantially reduced, to a level of $< 10\%$ near the central 15×15 mm of the beam (approximately the size of the CCD array). This *global* uniformity of the new homogenized anneal pattern was good enough that we decided to go ahead with a new anneal attempt using a 1×10^{15} cm^{-2} implanted device wafer.

5 RESULTS

5.1 CCD Noise, Gain and Dark Current

CCD noise and gain were measured with the system described in §3 using the techniques described in (Walton *et al.* 1985). The CCD noise for both lots 1229 and 1302 ranged from $\approx$ 15-20 e^- RMS with a system gain of 4.5-5 e^-/DN. The gain corresponds to an on-chip amplifier gain of $\approx$0.5-0.6 $\mu V e^-$. The noise is somehat higher than that usually associated with the TK512CB device, and may be attributable in part to the combination of low on-chip gain and a electrically noisy environment (turbopump controllers, etc.). In addition, the devices from this wafer lot were not screened for low noise characteristics or, for that matter, for especially good cosmetic quality or a partcularly low number of traps or bad columns: these characteristics, while important for a CCD for astronomical observing, are of relatively little import for the QE measurements described here. For the purposes of our QE measurements, the noise was of no consequence.

The CCD dark current was measured at -70 C to have a typical value $\lesssim 0.5e/pix/s$. This corresponds to a room-temperature (300K) equivalent of $\lesssim$ 1.0 nA cm^{-2} for the 27 μm CCD pixels. No special scheme for the vertical clocks was used to achieve this dark current level, except for holding 2 clock phases inverted at at -8 V during exposure. We thus find no evidence for an enhanced dark current in the implanted devices, suggesting that the Si/native oxide interface at the back surface is isolated from the CCD wells and that the dark current is primarily the result of the usual Si/oxide interface charge generation near the front of the CCD wells and the bulk Si dark current

5.2 Quantum Efficiency Table

In Table 2 we provide a summary of the quantum efficiency measurements for devices from lot 1302 for various wavelengths from the X-ray to the near IR. For all measurements, statistical uncertainties in either the measured charge in the CCD or the measured count rates in the reference detectors were always $\lesssim$ 2% for even the weakest lines, and much less for the stronger lines. Hence the uncertainties in the absolute QE (for the purpose of modeling the charge collection eficiency) are dominated by uncertainties in the reference detector calibration ($\sim$5-10%), effects of any CCD nonuniformity, and any systematic effects in the calibration process itself.

5.3 Spatial Uniformity at UV Wavelengths

In Figure 4 we show a 2537Å flat field for device 1302-7-9, annealed at an average energy density of 1.3 J cm^{-2}. Note that the global uniformity of the device is considerably improved over that from 1229-7-2. However, there are still optical patterns from incomplete homogenization of the laser beam, as discussed earlier. These focusing patterns, or caustics, are much more apparent as seen in the flat field image with a resolution of the 27 μm CCD pixel, compared to the much coarser ($\approx$ 800 μm) size of the Reticon pixel. For future work it is apparent that a newer, CCD-based laser anneal image system should be developed.

For comparison pusposes, we also provide in Figure 5 and Figure 6 similar flat-field measurements at wavelengths of 3650 and 4050 Å. The gradually increasing unifromity of the CCD images are due for the most part to the decreasing absorption coefficient at longer wavelengths. The respective 1/e absorption depths in silicon for 2537, 3650, and 4050 Å are, respectively, $\sim$ 60, 100, and 1000 Å.

5.4   Spatial Uniformity at EUV Wavelengths

For the quantum efficiency measurements detailed in the previous section, the nature of the ~mm size pencil beam and the relatively immobile relation between the CCD and the beam direction limited us to measurements of the QE over a relatively small area of the beam. However, an important consideration in the development of an EUV sensitive CCD is the overall spatial uniformity. To this end, we decided to examine the overall spatial uniformity of the CCD at a wavelength of 304 Å.

The apparatus used to illuminate the CCDs at this wavelength was developed for another program at Lockheed which involved calibration and assessment of CCDs produced for the Extreme Ultraviolet Imaging Telescope on the SOHO mission (De la Boudiniere *et al.* 1990). It consists of a hollow-cathode EUV source (the same as used for previous EUV quantum efficiency measurements), an aperture, a thin (~ 1500 Å) Al filter mounted on a mesh, and a Mo-Si multilayer flat designed to reflect He II 304Å radiation at an incidence angle of ~45°. The combination of Al filter and multilayer mirror provides both visible light rejection and elimination of other EUV line emission (such as He II 256 Å). The output beam, while not collimated, provides a relatively uniform monochromatic EUV light source over the surface of the CCD. By translating the CCD with respect to the output beam, we obtained a nearly "flat-field" response for the CCDs in the EUV, as can be seen in the image in Figure 7 . In this image, the overall RMS standard deviation of the illumination is $\sim 5\%$ or less, with large contributions coming from a relatively few low sensitivity areas produced as a result of the non-uniformities in the homogenized Nd:Glass laser beam used to anneal the CCDs. This strongly suggests that, with an improved beam homogenizer, very uniform response at this and other wavelengths should be possible with laser annealed, implanted CCDs.

5.5 Temporal Stability

The temporal stability of the laser annealed CCDs at UV wavelengths was tested by illuminating the devices with monochromatic light using the Hg lamp, interference filter and diffuser arrangement described earlier. We monitored device 1302-7-9 at 3 wavelengths (2537, 3650 and 4050 Å) over the course of $\sim$ 1 month. The Hg lamp source was chosen because of its inherent stability, relatively high illuminance (compared to the EUV sources), ease of obtaining frequent reference diode calibrations, and because the 3 UV lines span absorption path lengths of over a decade (from 60 Å for 2537 Å to over 1000 Å at 4050 Å). The device was cooled to -70 C before the start of a given daily run, and kept cold throughout the day. In addition, the device remained in high vacuum ($< 5 \times 10^{-8}$ torr) throughout the duration of the experiment. The results from this monitoring experiment are shown in Figure 8 , in which we plot the measured QE from each of 4 areas on the CCD as a function of time. For a given day, we derive sample std deviations of $\pm$ 1.0, 1.1, and 1.1 % RMS of the mean QE for each area at 2537, 3650, and 4050 Å. Over the course of several weeks, these measurements are reproducible to <2–3%. There is some suggestion of slight decline in the 4050 Å QE over the month-long period; however, it may be partly attributable to systematic errors at the 1–2% level.

5.6 QE Variation with Temperature

For devices from lot 1229, we conducted a series of tests to determine the variation of measured quantum efficiency at far UV wavelengths as a function of temperature. This was in part to see if any peculiarities in the CCD response occurred as a result of , for example, incomplete annealing of the impplanted region. This effect appeared to take place with excimer laser annealed devices produced in earlier implant/anneal experiments (Stern *et al.* 1989). We expect some variation due to changes in temeprature simply from the

various temperature dependences in the semiconductor properties such as diffusion length. The results of this experiment for device 1302-7-9 are shown in Figure 9 , in which we plot the quantum efficiency at three Hg lamp wavelengths as a function of temperature from -110 to -49 C. Note the gradual, yet calibratible decline in QE from -49 to -110C. The relative decrease ranges from 6%(4050 Å) to 18% (3650 Å) of the QE at -49 C.

Table 2: Measured Ion-Implanted/Laser-Annealed CCD Quantum Efficiency

			Device S/N	
λ	Source	Ref. Det.	1302-7-9	1302-7-12
13.3	Manson	PPC	0.91	0.93
23.6	Manson	PPC	0.80	0.80
44.7	Manson	PPC	0.48	0.46
67.6	Manson	PPC	0.32	0.30
114.	Manson	PPC	0.42	0.37
135.5	Manson	PPC	0.86	0.85
171.4	Manson	PPC	0.82	0.80
256.	HCD/He	MCP	0.60	0.61
303.8	HCD/He	MCP	0.58	0.57
461.	HCD/Ne	MCP	0.53	0.54
584.	HCD/He	MCP	0.30	0.29
736.	HCD/Ne	MCP	0.085	0.081
1215.5	HCD/H_2	MCP	0.055	0.054
2537.	Hg lamp	UDT UV-100	0.06	0.070
3500.	W-halogen	UDT	0.13	0.12
3650.	Hg lamp	UDT UV-100	0.09	0.10
4000.	W-halogen	UDT	0.33	0.32
4050.	Hg lamp	UDT UV-100	0.29	0.30
4500.	W-halogen	UDT	0.50	0.50
5000.	"	"	0.53	0.51
5500.	"	"	0.62	0.62
6000.	"	"	0.63	0.64
6500.	"	"	0.65	0.65
7000.	"	"	0.65	0.66
7500.	"	"	0.65	0.66
8000.	"	"	0.61	0.61
8500.	"	"	0.47	0.48
9000.	"	"	0.33	0.34
9500.	"	"	0.21	0.21
10000.	"	"	0.19	0.19

17

6 CCD QUANTUM EFFICIENCY MODEL

6.1 Overall Approach

Over the past decade, considerable effort has gone into modeling the quantum efficiency of pn-type solar cells using highly doped Si (Cuevas and Balbuena 1989, Bisschop *et al.* 1990); more recently, this modeling approach has also been applied to ion-implanted, backside illuminated CCDs (Bailey *et al.* 1990, Blouke 1991, Hochedez 1992). Such detailed modeling can, in principle, accurately describe the physical conditions in the back-illuminated, ion-implanted CCD. One disadvantage of this approach is that, in order to solve the charge transport and diffusion equations (see below), the precise form of the activated implant charge carrier density must be known, along with a set of parameters describing the minority carrier lifetime, etc. Such parameters may be known only imprecisely for a given CCD. Thus if we attempt to fit actual data to such models using only a narrow range of, e.g., optical wavelengths *with a correspondingly narrow range in Si absorption depth*, too many parameters and too few data points will result in poorly constrained models and little added physical insight into the overall CCD response.

By contrast, the QE results of the previous section provide strong constraints over nearly 3 decades in wavelength (13–10000 Å), corresponding to nearly 4 decades in Si absorption path ($\approx$60Å–50 μm). Consistency of the charge collection model can be checked by, e.g., comparing results for wavelengths in the X-ray and optical regimes having similar absorption paths. Our modeling approach combines a one-dimensional optical model for the CCD back surface and volume, and two alternative model formulations for the charge collection efficiency: a formal model involving solutions of the carrier density and continuity equations, and a semi-empirical model based on a simple linear form for the differential charge collection effiency. In the former case, the functional form and parameters for the implant are obtained from SIMS and spreading resistance measurements of similarly implanted and annealed test

wafers. It will be shown that the functional form of the charge collection efficiency in the CCD is almost identical for both types of models, given appropriate device parameters.

We assume that each photon which is absorbed in the active volume of the CCD creates 1 e-h pair per 3.65 eV of energy for photons with energy > 3.65 eV , and a single e-h pair for photons below this energy. To derive the probability for a photon of a given energy to be absorbed in the CCD active volume, we employ the LPARL multilayer model described in an earlier paper(Stern *et al.* 1986). Optical constants for Si and SiO_2 were obtained from Palik 1985. The oxide thickness and CCD depth (which are adjustable parameters) were estimated from measurements on similar CCD lots. We note that, given the high implant dose and consequent change in electrical conductivity of the implant region, the optical constants for the longer wavelengths may not be accurate. However, in the absence of an extended program to measure these constants from reflectivity and polarization mesaurements of the CCD surface, we have elected to use the standard set of optical constants for the modeling described here.

6.2 Fundamental Carrier Density and Continuity Equations: Formal Model

Using the basic physics of minority charge transport phenomena in semiconductors, the formal approach boils down to solution of the two coupled first-order linear differential equations (del Alamo and Swanson 1987):

$$J_n = qn_0 D_n \frac{\partial u}{\partial x}$$

$$\frac{\partial J_n}{\partial x} = -qG_L + n_0 \frac{q}{\tau_n} u$$

where J_n is the minority carrier current density in p-type Si, D_n is the diffusion coeffi-

cient, G_L the carrier generation rate, and the equilibrium electron concentration (assuming p doped material) is given by (Cuevas and Balbuena 1989):

$$n_0 = \frac{n_{io}^2}{N_A} exp(\frac{\Delta E_g^{app}}{kT})$$

and the variable u is defined as the normalized excess minority carrier density, i.e.:

$$u \equiv \frac{n - n_0}{n_0}$$

In general, *all* variables are functions of position within the material, and the semiconductor parameters are generally functions of temperature and dopant density (Cuevas and Balbuena 1989). Given *a priori* knowledge of the intrinsic minority carrier density n_{io}, the dopant distribution, N_A, the carrier lifetime, τ_n, the minority carrier mobility, μ_n, and the apparent bandgap narrowing, ΔE_g^{app}, all functions of the distance into the substrate, x, the above equations may be solved either numerically or analytically (Cuevas and Balbuena 1989) for the current density J_n for a given carrier generation rate G_L as a function of depth. At a given wavelength, G_L is merely the standard exponential photon absorption function, so the overall quantum efficiency may then be determined straightforwardly. The boundary conditions are derived from (1) the value of the surface recombination velocity (S_0)at the back surface:

$$J_n(x = 0) = qS_0n_0(0)u(0)$$

and (2) the boundary condition at the edge of the CCD depletion region:

$$u(x = d) = exp(\frac{qV}{kT}) - 1$$

where V is the voltage at the implant layer boundary. Varying V has a negligible effect on the derived charge collection efficiency, so we have arbitrarily set $u = 0 \Rightarrow V = 0$.

For purposes of comparison with the semi-empirical approach described later, we applied the above carrier transport equations using a heavily doped , backside illuminated CCD with a gaussian doping profile, a relatively good approximation to our SIMS and spreading resistance measurements. We then numerically solved these equations to derive the CCE as a function of depth in the CCD for a photon-produced charge generation function, G_L given by:

$$G_L = \alpha\phi(0)exp(-\alpha x)$$

and compared it for a variety of implant parameters. Examples of these calculations are shown in Figure 10 , in which we plot the integrated CCE for the doped region as a function of absorption path in the silicon for our best estimate of the implant distribution. The temperature is assumed to be -70 C. The different lines are labeled by different values for the most sensitive parameter, S_0. In the same figure, we also plot the measured CCE in the implant region, derived by correcting the measured QE for optical reflectivity and absorption. To avoid confusion, we have only plotted those data points taken at -70 C.

Each of the S-shaped curves in Figure 10 may be differentiated to form a *differential* CCE function: i.e., the probability that a charge created at a given depth in the CCD is collected in the CCD pixel. We show in the next section that, under the explicit assumption that the differential CCE is a linear function of depth, the QE for a back-illuminated CCD can be very well approximated by an analytic function whose parameters can easily be fit to measured QE data, and the parameters of this fit related, in turn to the (less well known) parameters of of the charge transport equations.

21

6.3 Semi-Empirical Model of CCD Quantum Efficiencies

For a typical shallow backside implant, the fraction of charge collected in the CCD wells from any given depth in the CCD pixel is a continuous function of distance from the back surface of the CCD. For photons absorbed very near the back surface, there must be some minimum amount of charge collected. For photons absorbed near the CCD wells, nearly all of the charge must be collected. The fraction of charge collected at intermediate distances is some function which is dependent upon the details of the implant distribution and the properties of the back surface. Interestingly enough, results of modeling such shallow implants suggest that this function may be nearly linear (Bailey *et al.* 1990).

We may *assume* that this function is indeed linear, and use actual measurements of CCD quantum efficiency to derive simple parameters for this relationship. Coupling the charge collection model to models for the optical properties of the CCD back surface and the conversion from photon energy to electron hole pairs, we may then derive a complete picture of the CCD response from the X-ray to the near -infrared. As with any model, this one has its limitations; however, as we shall see, it provides a surprisingly good picture of the CCD quantum efficiency over a wide range in energy.

The functional form of the charge collection efficiency (CCE) from the back surface is assumed to be of the following form:

$$CCE = \begin{cases} \eta_0 + (1 - \eta_0) * \frac{x}{W} & x < W \\ 1 & x > W \end{cases}$$

where W is the effective depth of the implant region, and η_0 the differential CCE at the back surface (both fit parameters).

When this is combined with the LPARL multilayer code (which calculates the reflectivity

of the back surface with a small amount of native oxide), and the absorption coefficient as a function of wavelength, the functional form for the CCD quantum efficiency is easily obtained by simple integration. This functional form is given by:

$$QE = T_\lambda[\eta_0(1. - exp(-z_0)) + (\frac{1 - \eta_0}{z_0})(1 - exp(-z_0)(1 + z_0))]$$

for the implanted region, where $z_0 = \alpha W$ and α = the absorption coefficient, W the implant "width" parameter, η_0 is the differential CCE at the back surface, and T_λ is the net transmission of photons through the back surface oxide after correcting for surface reflectivity.

The viability of this approach can be seen in Figure 11 which shows the measured (internal) quantum efficiency (IQE) of the CCD, and the CCE model, after reflection losses have been taken into account, against the absorption length at a given wavelength. Each point is labeled by the wavelength. Note that at very small absorption paths the minimum IQE reaches an asymptotic value largely determined by the surface recombination velocity, and at very large absorption paths approaches 100% as expected.

Another way of looking at this is to compare the model QE's (including reflectivity) with the observed QE's. In this case, we also include a correction for photons which are lost via transmission through the entire CCD substrate. This is shown in Figure 12 . Here we also include those points taken at room temperature in diode mode. Note that the diode mode data at long wavelengths (and at room temperature) is consistently underestimated by the fit above $\lambda \approx 5000$ Å. We may, in turn, use *all* the data, including those taken in diode mode at room temperature, to constrain the best fit semi-empirical model. The results of this fitting procedure in shown in Figure 13 . Note that the diode mode data are well fit, resulting in a somewhat poorer fit for some of the data points in the X-ray regime. However, the only parameter significantly affected is the substrate depth, as might be expected. It is likely that the combination of room T operation and, perhaps more significantly, the use of

23

diode mode data has resulted in collection of charge beyond the nominal CCD well depth. Another possibility is the effect of internal reflections at long wavelengths, which are not accounted for in the present model.

In any event, the parameters of the implnated region are relatively insensitive to the inclusion or exclusion of the diode mode data. It is surprising, and encouraging, that a few simple assumptions regarding CCE can produce a model which fits the -70 C data remarkably well. The model parameters can in turn be used to estimate constraints on physical parameters such as surface recombination velocity, and carrier lifetime.

7 DISCUSSION

For the shallow, highly doped laser annealed implants we have used, both the semi-empirical model and the formal solution of the carrier density and continuity equations provide nearly equivalent approximations to the actual measured CCE. The semi-empiricaal model has the advantage that it may be easily fit to experimental data. Hence it provides a useful analytic functional form which is simple to incorporate into a model of the CCD response with wavelength. This in turn may be incorporated into a model of CCD response to predict the properties of CCD-based detector systems in X-ray, EUV, or UV telescopes, or as part of an overall telescope response model derived from CCD calibration data. The parameters used in the model, η_0 and W, provide useful indications of the implant's surface properties and effective width, although they do not correspond exactly to the commonly used parameters in semiconductor modeling.

On the other hand, the formal solution of the carrier density and continuity equations allows a comparison between, on one hand, the semi-empirical model parameters, and, on the other, to physical properties of the semiconductor surface and implant regions. From our solution of theses equations, and the fitting of parameters to our QE measurements, we have seen that the largest effect on the QE at UV wavelengths is the apparently high surface recombination velocity (S_0) of the annealed surface. This is understandable in light of the fact that no attempt was made to further passivate the back surface of the CCD beyond the laser anneal itself: hence the Si/oxide interface at the back surface, while it no longer controls the potential deep in the CCD substrate (because of the high carrier concentration of the implant), nevertheless is a place of high charge recombination. The implants we have used, under the assumption that they have been fully annealed, are shallow enough that the effects of recombination in the implant itself should not be a major factor in the CCD QE. This can be seen by noting that the diffusion length in of minority carriers in implanted

25

p+ Si for the carrier concentrations studied (10^{19-20} cm^{-3}) is > 6000 Å, even at 200 K and the highest implant level, and is typically $\sim 1\ \mu m$ or more. In our 1-D model, charge must either: (1) recombine at the surface, (2) recombine in the implant, or (3) be collected in the CCD well. Since (2) is unimportant because the scale for the difusion length is $\gtrsim 10$ times that of the gaussian width of the implant, our incomplete charge collection must result from a high $S \gtrsim 5 \times 10^5 cms^{-1}$.

Thus, the simplest way to improve the CCE for the short absorption path photons would be to passivate the back surface of the CCD *after* the laser anneal. An oxide coating would be one way to do this; however, to maintain the EUV and far UV QE, it would have to be extremely thin. In the optical region, this would not be an issue. In the UV, the use of anti-reflection coatings, as is being pursued in other programs would significantly increase the absolute QE of the CCD; however, unless the same AR coating also served to passivate the back surface, incomplete charge collection would still occur.

8 SUMMARY

The results of our QE measurements and modeling have, we believe, produced a consistent physical decription of the photon absorption and charge collection process in our CCDs. In addition, our experimental results have demonstrated that implanted, laser-annealed CCDs produced using our process can be practically fabricated on the wafer scale. We draw the following conclusions from our results:

- We have demonstrated High QE in the optical, X-ray and EUV without special coatings, etc.;

- The UV QE is limited by reflection and surface recombination.

- The devices work well in hard vacuum and at temperatures down to at least -110 C and have a slow and calibratable change in QE as a function of temperature.

- The devices are stable to within a few % in QE over long periods ($\sim$ 1 month), and in high ($\sim 4 \times 10^{-8}$ torr) vacuum.

- The device uniformity is good, with any nonuniformity is directly traceable to the non-uniformity in the laser homogenizer pattern.

REFERENCES

P. Bailey, C. Castelli, M. Cross, P. van Essen, A. Holland, F. Jansen, P. de Korte, D. Lumb, K. McCarthy, P.Pool, and P. Verhoeve, "Soft X-ray performance of back-illuminated EEV CCDs," in *EUV, X-Ray, and Gamma-Ray INstrumentation for astronomy and Atomic Physics*, Proc. SPIE, 1384 (1990).

F.J. Bisschop, L.A. Verhoef, and W.C. Sinke, "An analytical solution for the collection efficiency of solar cell emitters with arbitrary doping profile," IEEE Trans. Electron Devices, 37, 358 (1990).

M.M. Blouke, "Model of a thinned CCD," SPIE Proc [?] (1991?)

J.T. Bosiers, N.S. Saks, D. McCarthy, M.C. Peckerar and D.J. Michels, "CCDs for high resolution imaging in the near and far UV," in *Ultraviolet Technology*, R.E. Huffman, ed., Proc. SPIE 687, 126–135 (1986).

A. Cuevas and M.A. Balbuena, "Review of Analytical models for the study of highly doped regions of silicon devices," IEEE Trans. Electron Devices, 36, 553 (1989).

A.G. Cullis, H.C. Webber, and P. Bailey, " A device for laser beam diffusion and homogenisation," J. Phys. E., 12, 688 (1979).

J.A. del Alamo and R.M. Swanson, "Minority transport in heavily doped silicon: fundamental equations," Japanese Journ. Appl. Phys., 26, 1860 (1987).

J.P. Delaboudiniere *et al.* , "The Extreme Ultraviolet Imaging Telescope on board SOHO," SPIE Proc., 1160, 518, (1989).

J.F. Hochedez, 1992, in preparation.

J.R. Janesick, T. Elliott, T. Daud, J. McCarthy, and M. Blouke, "Backside Charging of the CCD,", SPIE Proc. 570, 46 (1985).

J.R. Janesick, D. Campbell, T. Elliott, and T. Daud, "Flash technology for charge-coupled device imaging in the ultraviolet," *Opt. Eng.* 26 (9), 852–863 (1987).

J.R. Janesick, T. Elliott, S. Collins, M.M. Blouke, and J. Freeman, "Scientific charge-coupled devices," *Opt. Eng.* 26(8), 692–714 (1987).

J.S. Katzeff, M. Lopez, and D.R. Burger, "Laser processing of silicon solar cells," in *Proceedings of the IEEE 15th Photovoltaic Specialists Conference*, p. 437 (1981).

J.E. Manson, "Light source and filters for use in the 130–280 Å region," Appl. Opt., 12, 1394 (1973).

A. Palik, *Handbook of Optical Constants of Solids* , Academic Press, N.Y. (1985).

F. Paresce, S. Kumar, and S. Bowyer, "A continuous discharge line source for the extreme ultraviolet," Appl. Opt. , 10, 1904 (1971).

J.M. Poate and J.W. Mayer, eds. "Laser Annealing of Semiconductors," Academic Press, New York (1982).

L. Shing and R. Stern, "Development of a low contamination camera head for the evaluation of CCDs in the UV and EUV," Proc. SPIE, 1344, 396 (1990).

R.A. Stern, R.C. Catura, M.M. Blouke, and M. Winzeneread, "EUV astronomical spectroscopy with CCD detectors," in *Instrumentation in Astronomy VI*, D.L. Crawford, ed., Proc. SPIE 627, 583–590 (1986).

R.A. Stern, R.C. Catura, R. Kimble, A.F. Davidsen, M. Winzenread, M.M. Blouke, R. Hayes, D.M. Walton, J.L. Culhane, "Ultraviolet and extreme ultraviolet response of charge-coupled-device detectors," *Opt. Eng.* 26(9), 875–883 (1987).

R.A. Stern, T. Whittemorre, M. Winzenread, and M.M. Blouke, "Ultraviolet quantum efficiency and vacuum stability of ion-implanted, laser annealed CCDs," in *Optical Sensors and Electronic Photography*, Proc SPIE, 1071, 43 (1989)

C. Tassin, Y. Thenoz, R. Le Maitre, and J. Chabbal, "Thinned Backside Illuminated CCDs for Ultraviolet, Soft X-Ray and Electron Beam Imaging," Proc. SPIE, 1140, xx, (1989).

D. Walton, R.A. Stern, R.C. Catura, and J.L. Culhane, "Deep-depletion CCDs for x-ray astronomy," in *State-of-the-Art Imaging Arrays and Their Applications*, K.N. Prettyjohns, ed., Proc. SPIE 501, 306–316 (1984).

D.L. Windt and R.C. Catura, "Multilayer caharacterization at LPARL," in *X-Ray Multilayers for Diffractometers, Monochromators and Spectrometers* , Proc. SPIE, 984, 82 (1988).

R.T. Young, C.W. White, G.J. Clark, J. Narayan, W.H. Christie, M . Murakami, P.W. King, and S.D. Kramer, "Laser annealing of boron-implanted silicon," Appl. Phys. Letters., 32(3), 139 (1978).

Figure Captions

Figure 1 Schematic diagram of LPARL Calibration Facility.

Figure 2 Gray scale image of 2537 Å flat-field for device 1229-7-2 with overlay of laser anneal energy density contours in J cm^{-2}. In gray scale image, darker indicates higher response. The white region at the extreme right of the image is due to a improperly aligned anneal mask.

Figure 3 Energy density contours of improved homogenizer output. Approximate size of CCD active area is shown by dashed box.

Figure 4 2537 Å flat field image for device 1302-7-9. Line plot shows response for indicated row number.

Figure 5 3650 Å flat field image for device 1302-7-9.

Figure 6 4050 Å flat field image for device 1302-7-9.

Figure 7 304 Å flat field image for device 1302-7-9.

Figure 8 QE vs. time for device 1302-7-9 for 4 regions on the CCD and at wavelengths of 4050 ($\sim$ 28-30%), 3650 ($\sim$ 8%), and 2537 Å($\sim$ 6%).

Figure 9 Mean QE vs. temperature for device 1302-7-9 at 3 wavelengths indicated.

Figure 10 The integrated CCE vs 1/e absorption depth (Å) calculated using the carrier density and continuity equations for a range of S_0. In all cases N_A (peak) = 1.0×10^{20}, Implant gaussian width = 500 Å, Implant peak = 100 Å, T=200K. Also shown is the measured integrated CCE using data for device 1302-7-9 and assuming a 50 Å oxide layer (sqaures with wavelengths indicated).

Figure 11 Measured integrated CCE using data for device 1302-7-9 and assuming a 50 Å oxide layer (sqaures with wavelengths indicated). The best fit semi-empirical model is shown by the dotted line. Best fit parameters are: $\eta_0 = 0.21$, $W \approx 2300$ Å.

Figure 12 Measured QE for device 1302-7-9 (Open Diamonds = data taken at -70 C; filled diamonds = data taken at room T in diode mode). Maximum theoretical QE for 100 % CCE (dotted line). Best fit semi-empirical model using only -70 C data (solid line).
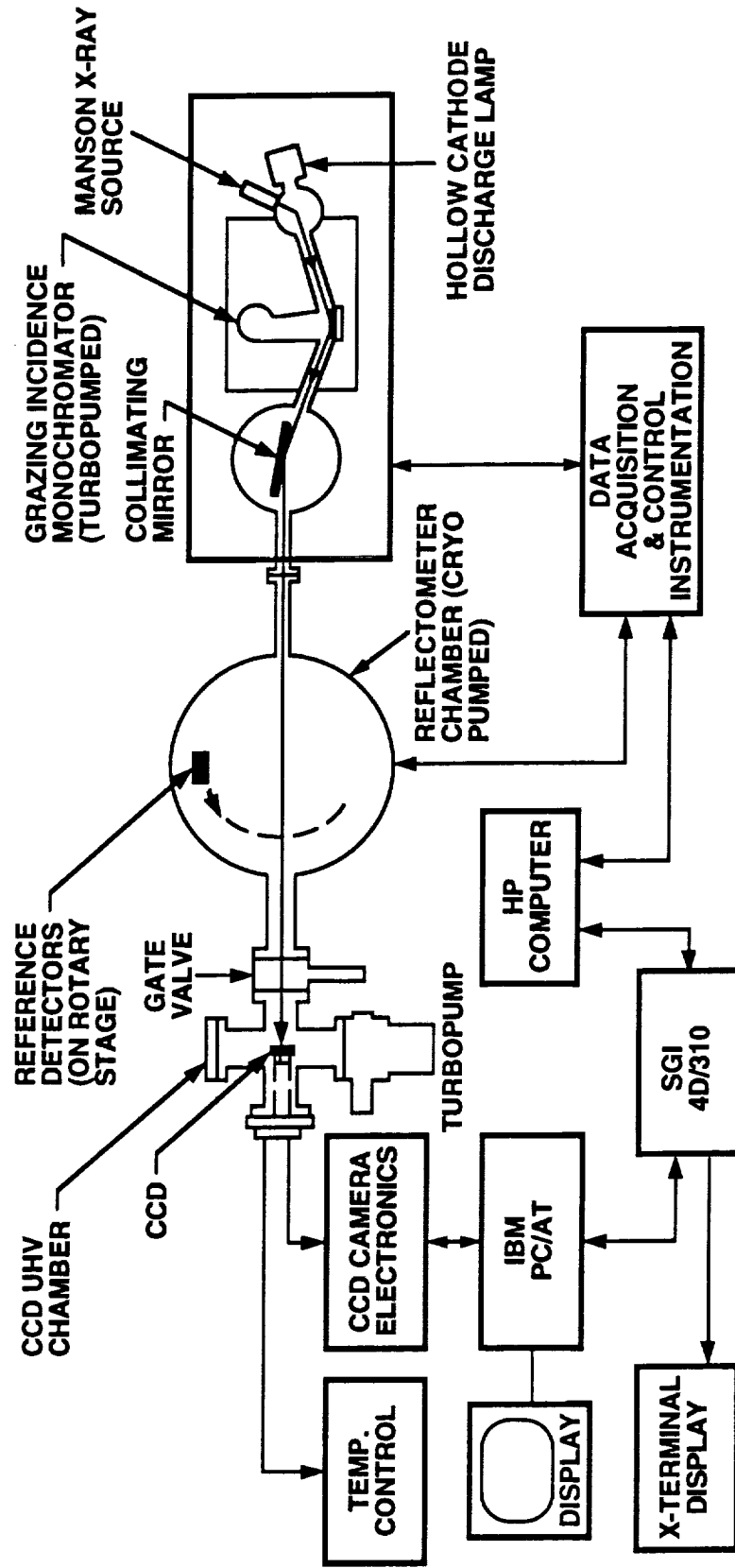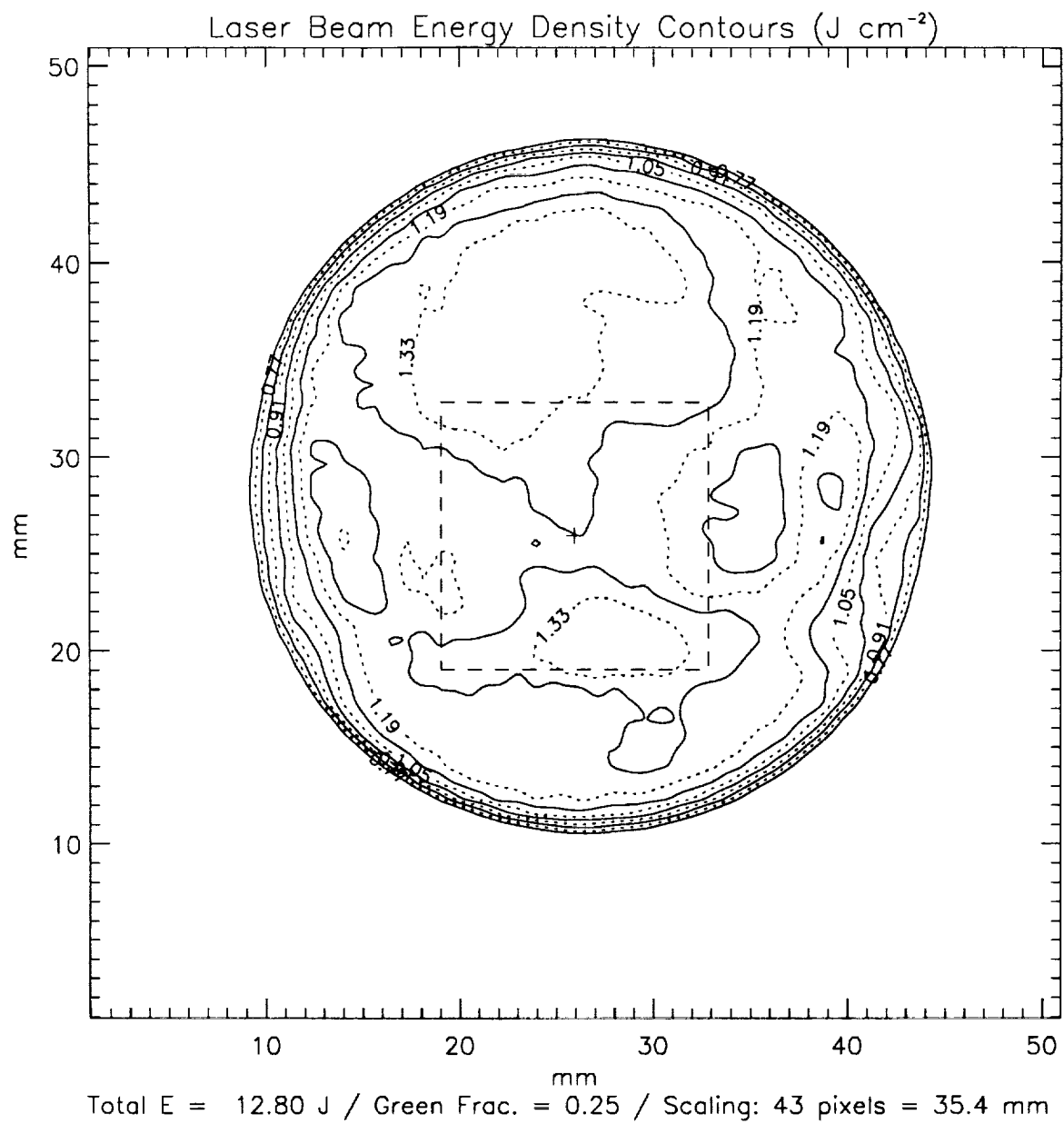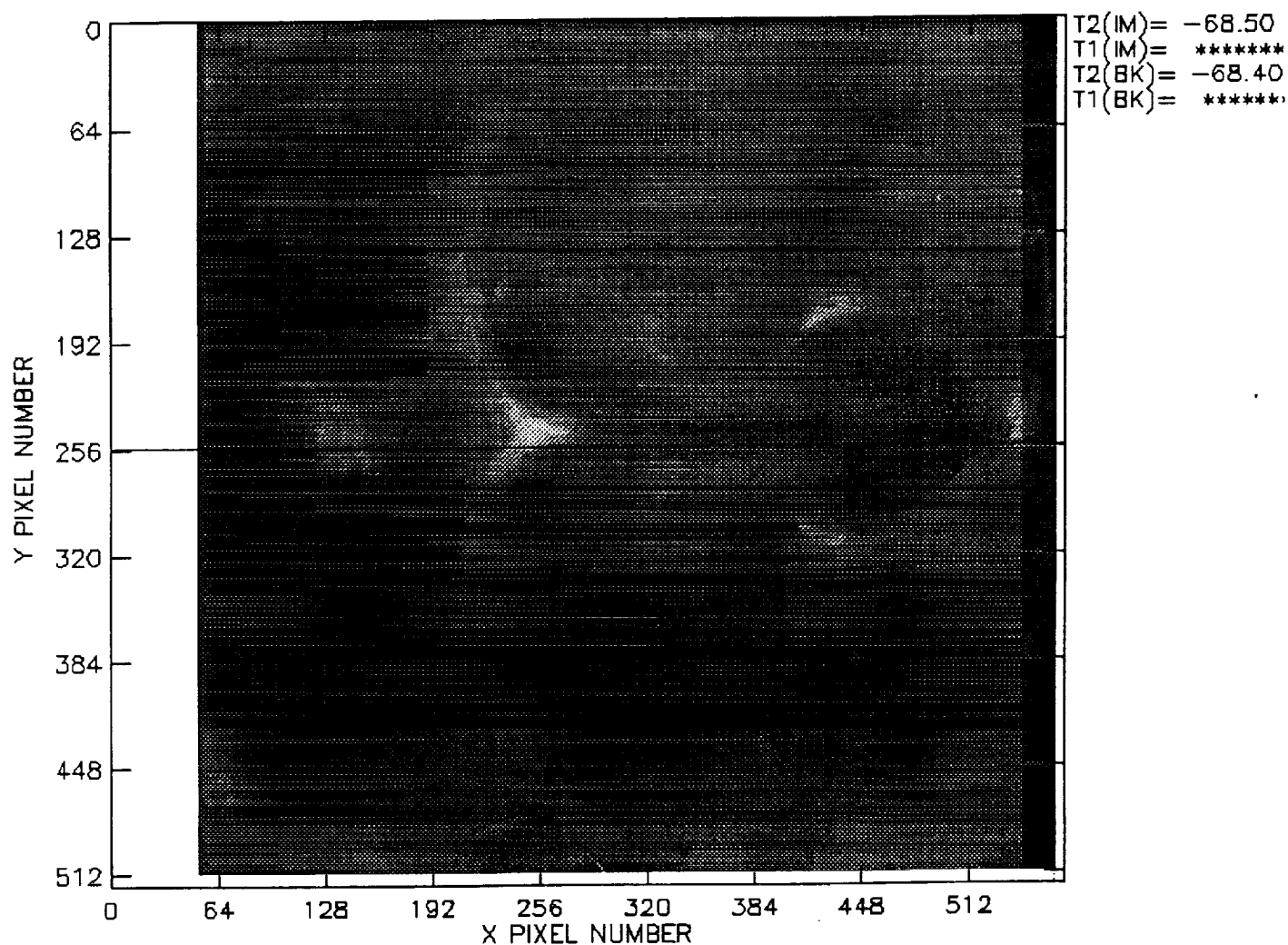
Figure 13 Measured QE for device 1302-7-9 (Open Diamonds = data taken at -70 C; filled diamonds = data taken at room T in diode mode). Maximum theoretical QE for 100 % CCE (dotted line). Best fit semi-empirical model using all data (solid line).

MANSON X-RAY SOURCE

GRAZING INCIDENCE MONOCHROMATOR (TURBOPUMPED)

COLLIMATING MIRROR

HOLLOW CATHODE DISCHARGE LAMP

REFLECTOMETER CHAMBER (CRYO PUMPED)

REFERENCE DETECTORS (ON ROTARY STAGE)

GATE VALVE

CCD UHV CHAMBER

CCD

TURBOPUMP

DATA ACQUISITION & CONTROL INSTRUMENTATION

HP COMPUTER

SGI 4D/310

CCD CAMERA ELECTRONICS

IBM PC/AT

TEMP. CONTROL

DISPLAY

X-TERMINAL DISPLAY

FIG. 1

FIG. 2

Laser Beam Energy Density Contours (J cm^{-2})

Total E = 12.80 J / Green Frac. = 0.25 / Scaling: 43 pixels = 35.4 mm

FIG 3

LINE NUMBER =   255

Quantum Efficiency

X PIXEL NUMBER

Y PIXEL NUMBER

X PIXEL NUMBER

T2(IM)= −68.50
T1(IM)= *******
T2(BK)= −68.40
T1(BK)= ******

DEVICE 1302-7-9. 10 SEC EXP. AT 2537A. 16:40 9/26/91

DEVICE 1302-7-9. 10 SEC DARK EXP. 16:41 9/26/91

FIG 4

LINE NUMBER =   255
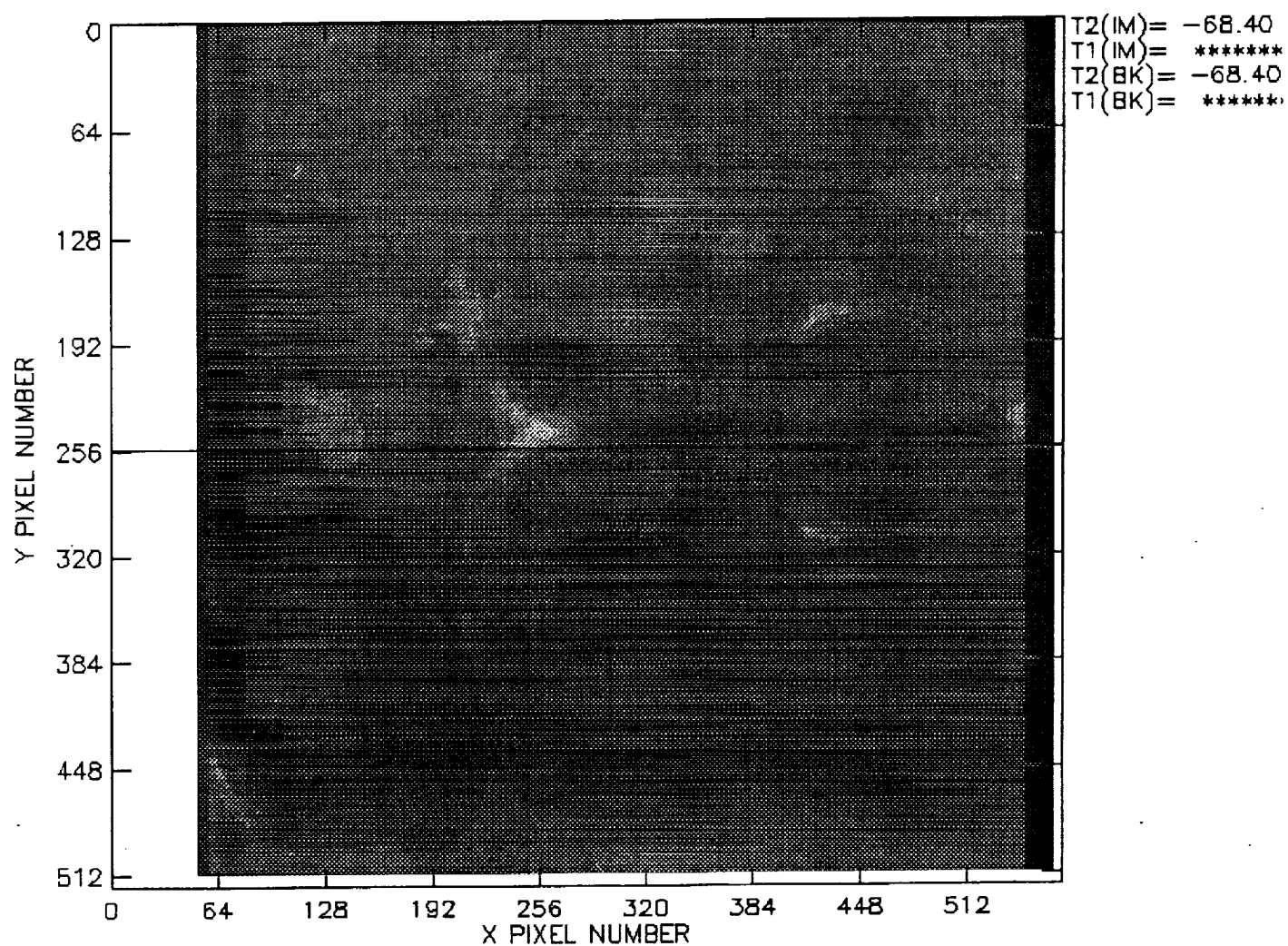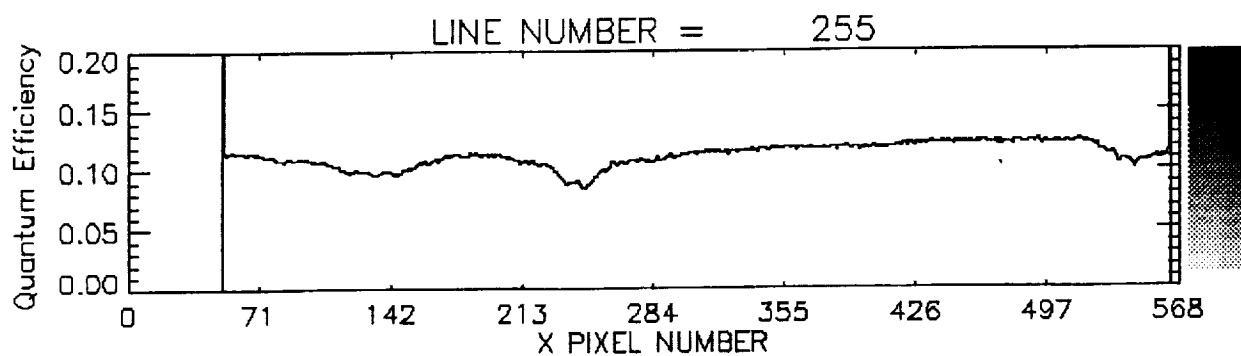
DEVICE 1302-7-9. 10 SEC EXP AT 3650A. 16:51 9/26/91

DEVICE 1302-7-9. 10 SEC DARK EXP. 16:41 9/26/91

FIG. 5

LINE NUMBER =   255

Quantum Efficiency

0.40
0.30
0.20
0.10
0.00

0   71   142   213   284   355   426   497   568
X PIXEL NUMBER

T2(IM)= −68.30
T1(IM)= ******
T2(BK)= −68.30
T1(BK)= ******

Y PIXEL NUMBER

0
64
128
192
256
320
384
448
512

0   64   128   192   256   320   384   448   512
X PIXEL NUMBER
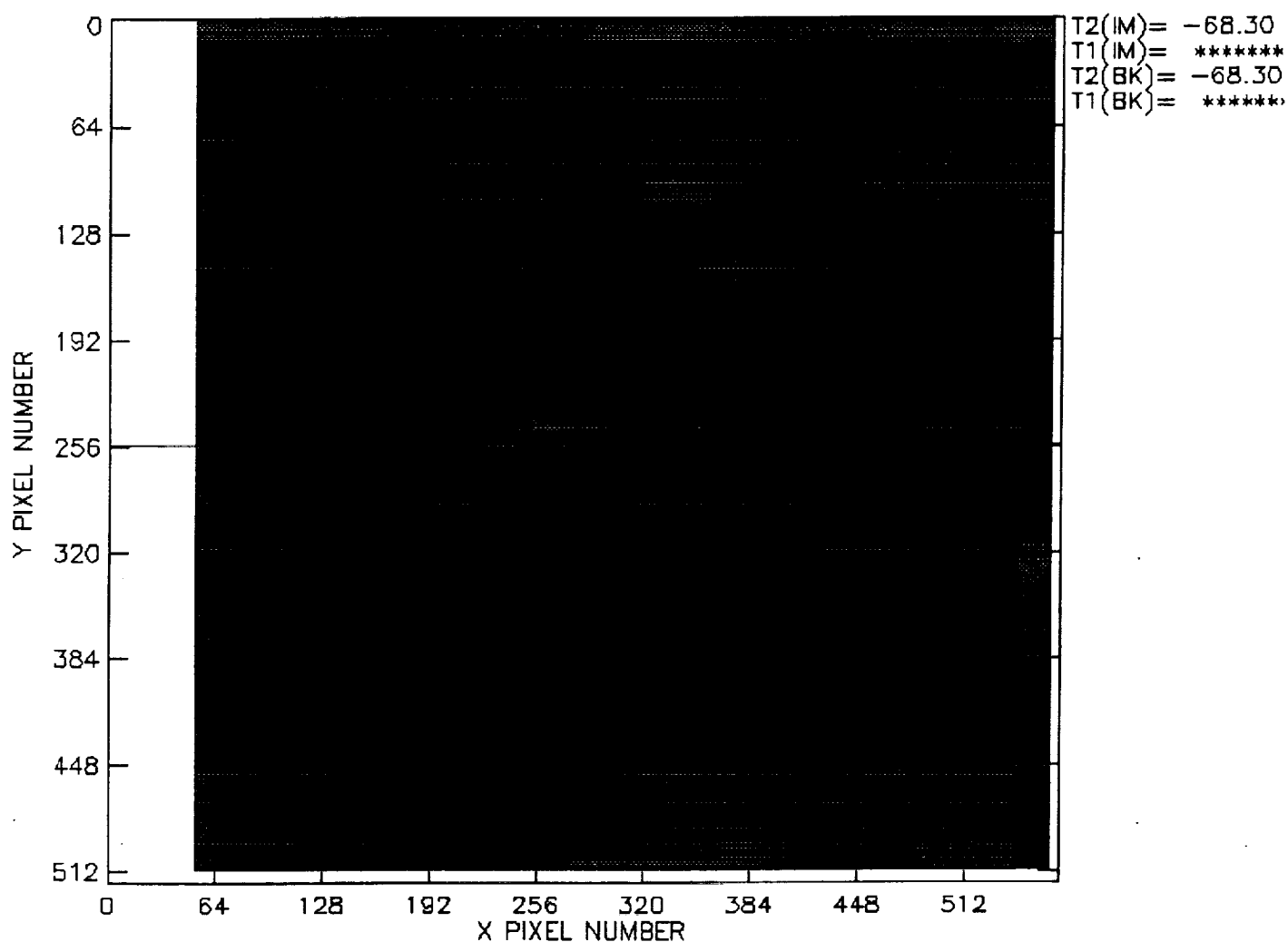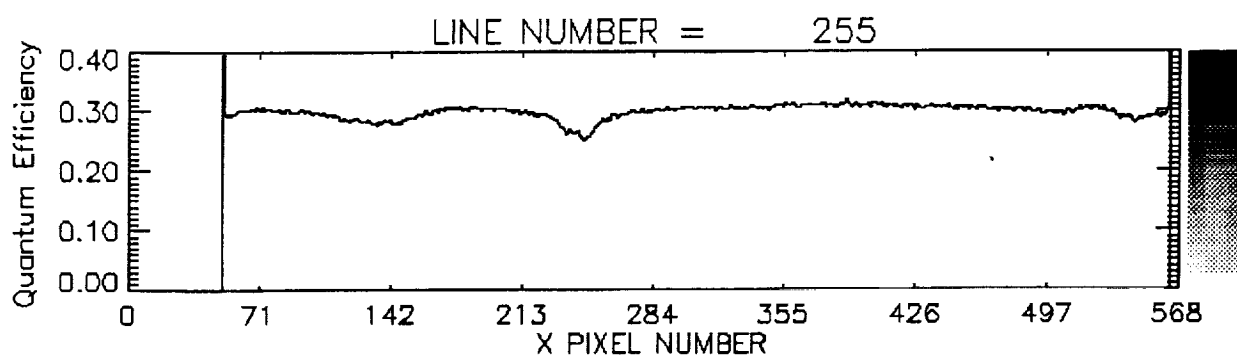
DEVICE 1302−7−9. 10 SEC EXP AT 4000A. 16:57 9/26/91

DEVICE 1302−7−9. 10 SEC DARK EXP. 16:58 9/26/91

FIG.6

LINE NUMBER =   200
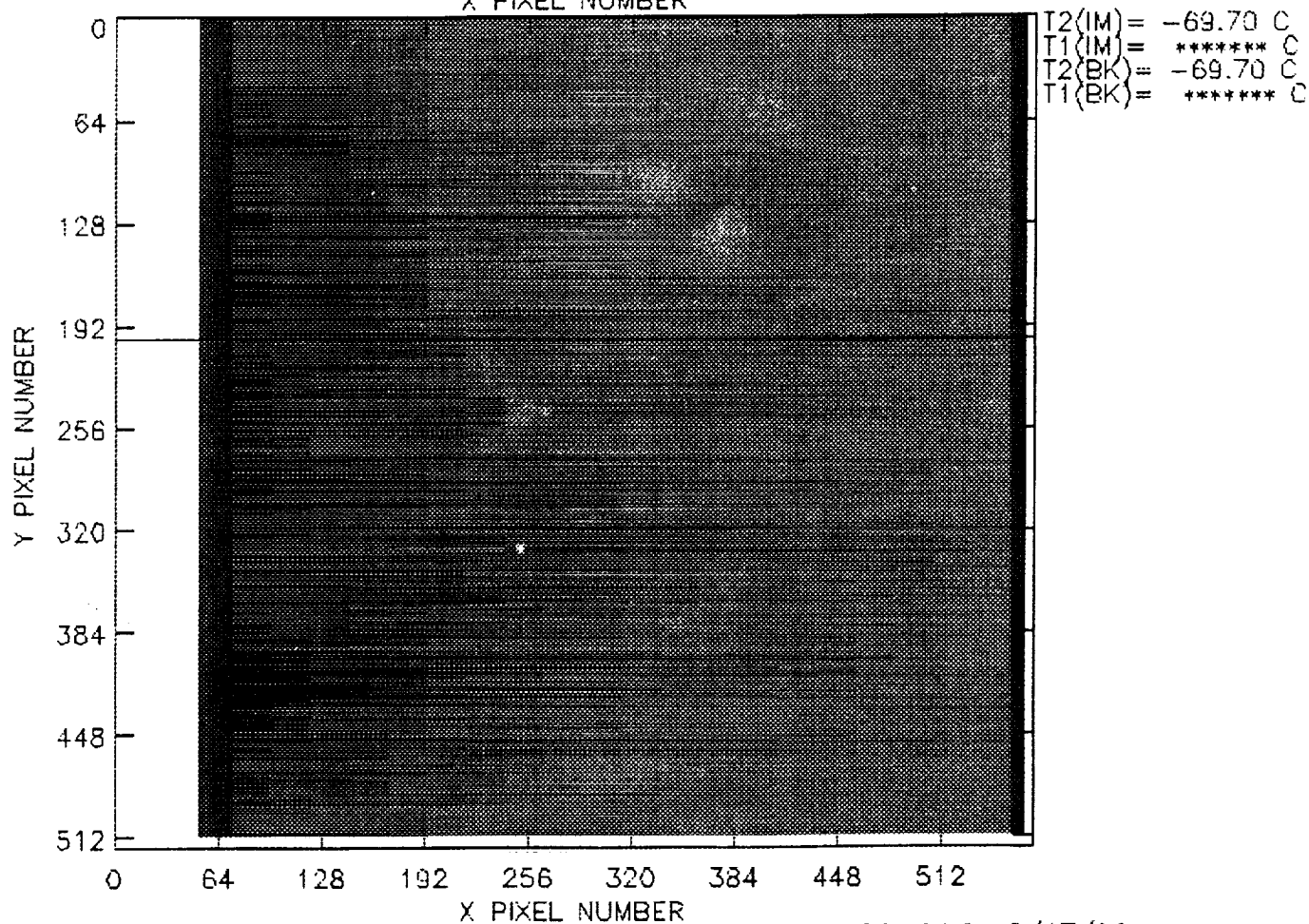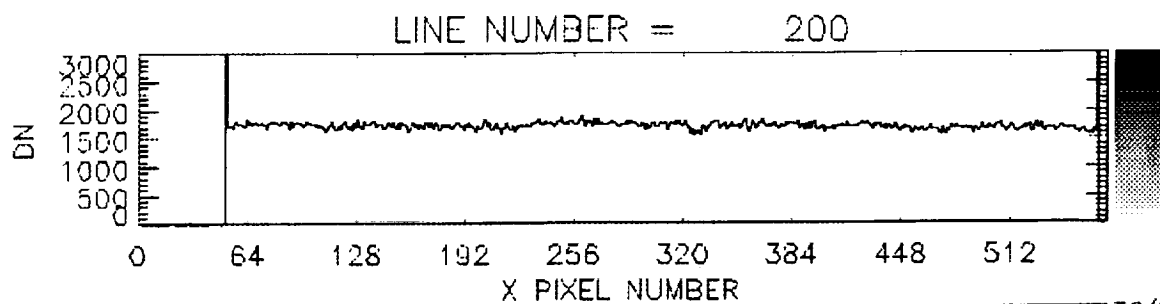
DEVICE 1302-7-9. 20 SEC EXP. He 304A. X=+0.3" Y=0.0" 14:24 8/17/92

DEVICE 1302-7-9. 20 SEC DARK FRAME 13:55 8/17/92

FIG 7

FIG.9

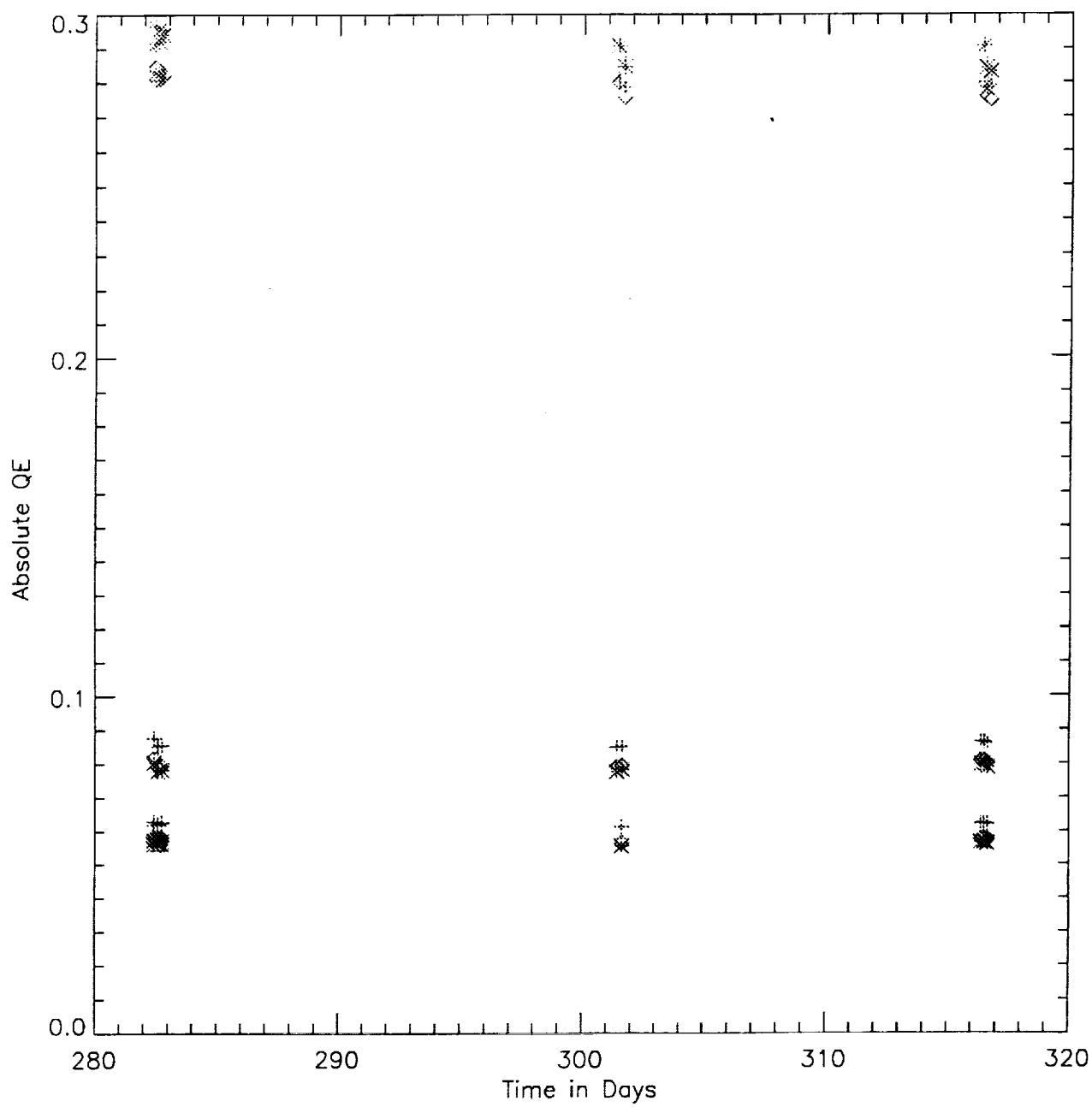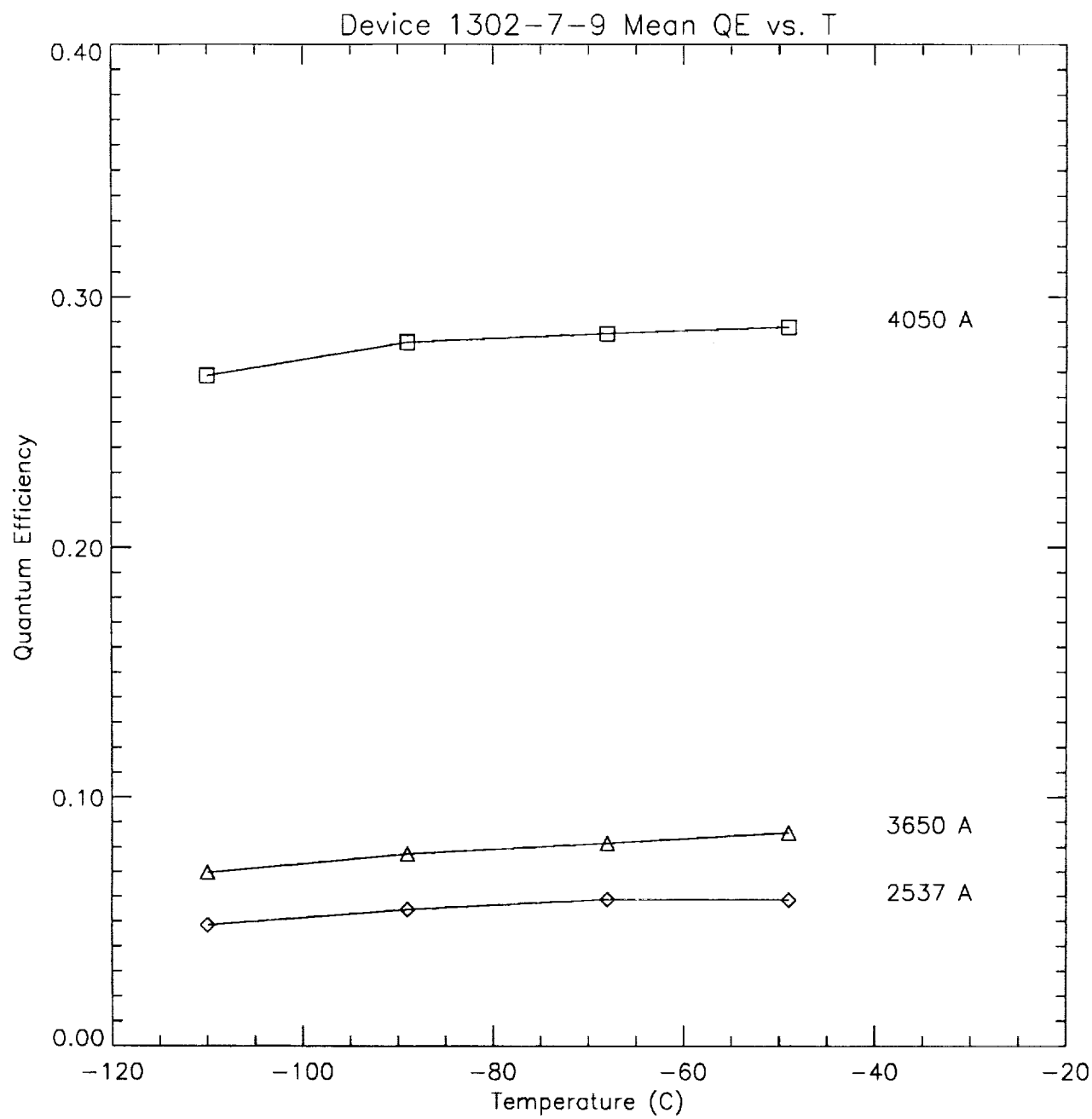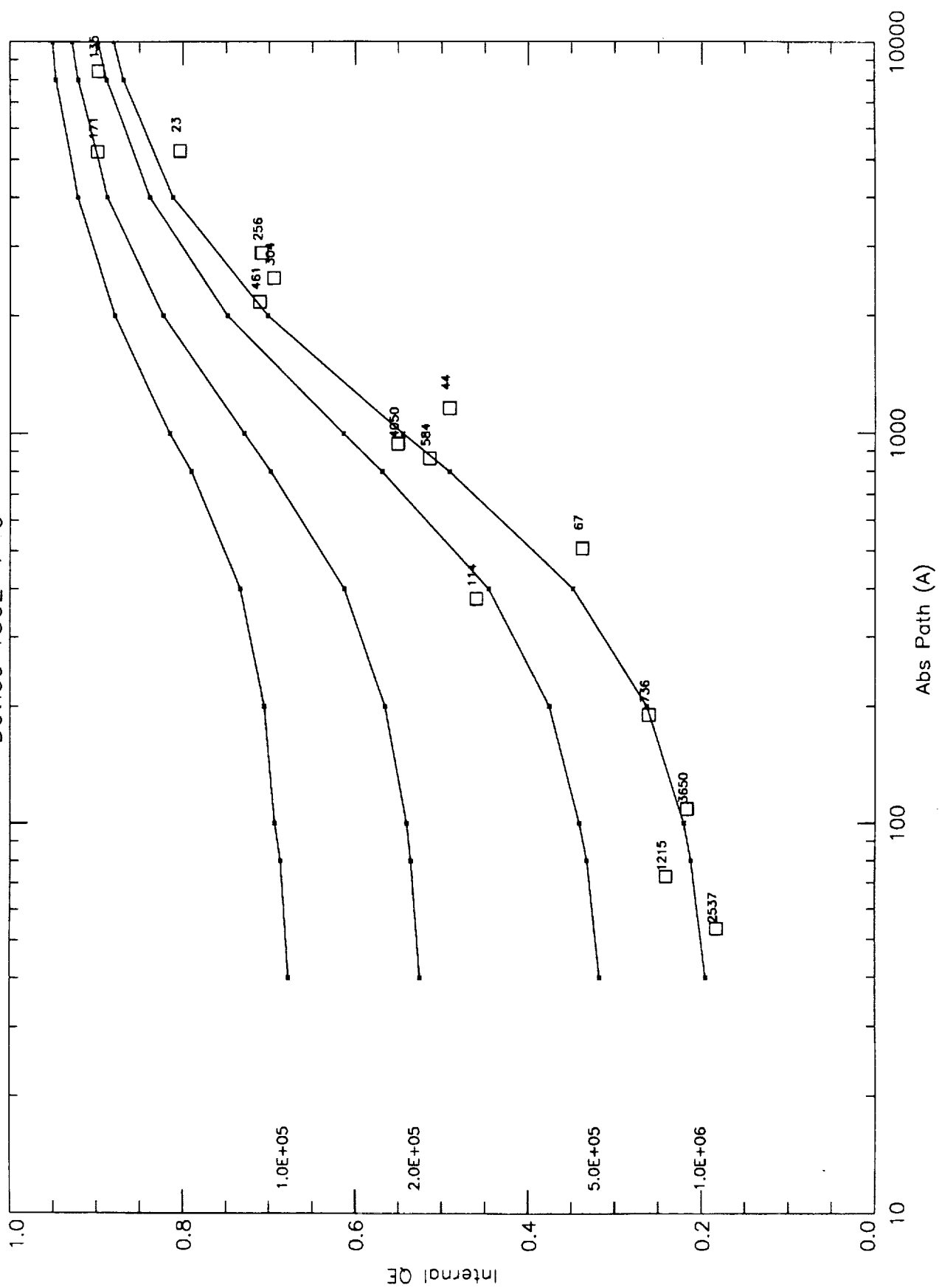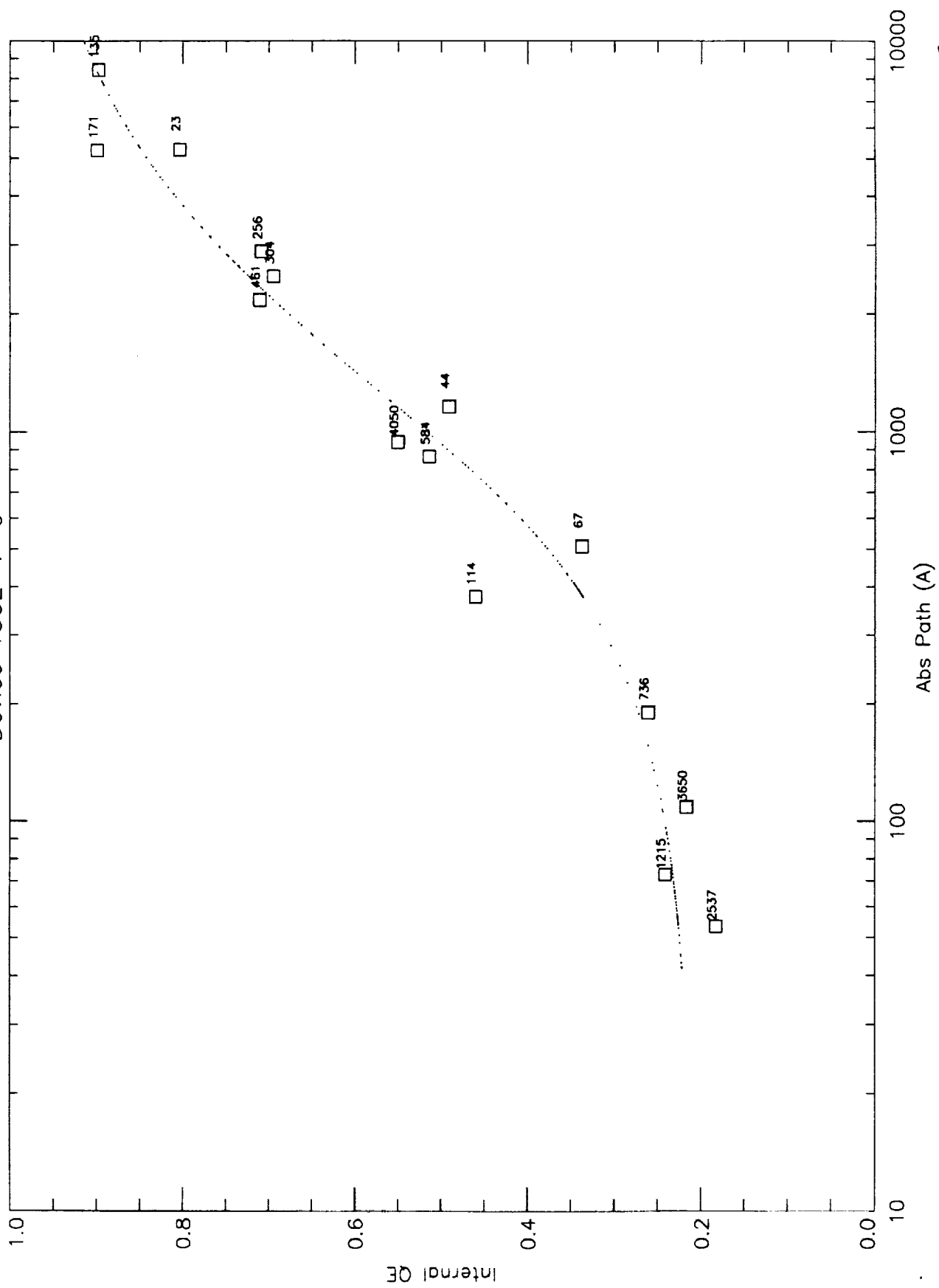Device 1302-7-9 Mean QE vs. T

FIG.9

Device 1302-7-9

FIG 10

Device 1302-7-9

Internal QE

Abs Path (A)

FIG. 11

Device 1302-7-9

QE

1.0

0.8

0.6

0.4

0.2

0.0

10   100   1000   10000

Wavelength(A)

Surface Depletion Region (A):   0.

Surface Oxide Layer (A):   50.

Implant Region (CCE < 1) (A):   2317.

Minimum CCE at Surface: 0.21

Substrate Depth (um):   7.

FIG.12

Device 1302-7-9

Surface Depletion Region (A):	0.
Surface Oxide Layer (A):	50.
Implant Region (CCE < 1) (A):	2090.
Minimum CCE at Surface:	0.23
Substrate Depth (um):	17.

Wavelength(A)

QE

FIG. 13